Materials and Structures (2025) 58:331
https://doi.org/10.1617/s11527-025-02825-4

ORIGINAL ARTICLE

Tensile characterization of high-performance fibre-reinforced concrete: effect of steel or amorphous metallic fibres and of cement type

Francesco Lo Monte · Eduardo J. Mezquida-Alcaraz · Juan Navarro-Gregori · Pedro Serna · Liberato Ferrara

Received: 21 April 2025 / Revised: 12 September 2025 / Accepted: 7 October 2025

Abstract The need of more sustainable structures pushes ahead the formulation of new advanced cementitious materials which can significantly improve the structural durability, thus resulting into a longer service life with reduced maintenance. Within this framework, the research project ReSHEALience (H2020 GA 760824) has developed a new approach for the design of structures exposed to extremely aggressive environments, starting from a novel concept of High-Performance Fiber-Reinforced Concrete (HPFRC). In a design perspective, this makes it necessary to effectively identify the main parameters describing the overall material behaviour in tension (this being instrumental also for the durability estimation in the cracked state). In the present study, starting from the results of 4-Point Bending Tests on small beams, an inverse-analysis identification procedure has been implemented in order to evaluate the response in direct tension in terms of stress–strain and stress-crack opening laws. The procedure has been implemented for three different HPFRC mixes differing in the type of fibre (straight steel or amorphous metallic ones) and of cement (CEM I or CEM III). The characterization procedure allowed to highlight the effect of fibre type on the whole response in direct tension in terms of loading–unloading response and post-peak regime. In this view, the study aims at further pushing forward the adoption of HPFRC in the design of structures, thanks also to the increasing awareness fostered by the most recent standards.

Keywords HPFRC · Tensile behaviour · Inverse analysis · Straight steel fibres · Amorphous metallic fibres · Cement type

F. Lo Monte (✉) · L. Ferrara
Politecnico Di Milano, Milan, Italy
e-mail: francesco.lo@polimi.it

E. J. Mezquida-Alcaraz · J. Navarro-Gregori · P. Serna
Universitat Politècnica de València, Valencia, Spain

1 Introduction

Sustainability is one of the keywords of the present century, this being instrumental in the view of a circular economy framework. In the last decades and, in particular, in the most recent years, big efforts have been made in improving the environmental impact of the whole construction industry value chain, mainly working at the material production level with reduction of the raw materials consumption and of the overall carbon footprint. In parallel, a further virtuous path addresses the issue at the structural level targeting a significant extension of the service life of structures and infrastructures, with a reduced need for maintenance and restoration interventions. This translates in demanding a higher material and structural durability, which, as a matter of fact, allows to reduce the cost and the environmental impact when the whole structural life cycle is considered [1–3].

Published online: 09 November 2025

This purpose represents the core goal of the Research Project ReSHEALience (GA 760824), launched in 2018 within the framework of the Research and Innovation Programme Horizon 2020, with the main objective to develop a durability-oriented structural approach for both ordinary and extremely aggressive environments. The explicit evaluation of key durability parameters is expected to foster a far more efficient exploitation of the huge benefits brought in by the most recent advanced cementitious materials [4, 5].

To this end, High and Ultra-High Performance Fibre-Reinforced Concrete (HPFRC and UHPFRC) represents a powerful tool on the hands of the designers, thanks to the positive interaction of reduced crack-opening and autogenous self-healing, which can lead to significantly increase the long-term performance in the cracked state, in ordinary and extremely aggressive environments.

FRCs, HPFRCs and UHPFRCs have been rather extensively studied in the last decades, concerning the behaviour at the Ultimate Limit State (ULS) [6–13], the effect of fibre orientation [14–17] durability in the un-cracked state, pumpability [18] and rheology [19, 20], while information is still needed at the Serviceability Limit State (SLS), especially regarding durability performance in the cracked state.

As it is well known, the tensile response of HPFRC and UHPFRC can be characterized by hardening behaviour in bending and/or in direct tension (deflection-hardening and strain-hardening behaviour, respectively), thanks to the stable propagation of multiple cracks after the onset of the first crack [21, 23] (and before the localization of a single unstable crack takes place). Such extensive multiple cracking characterized by very small cracks makes it very effective the autogenous self-healing processes, as attributed, among other reasons, to the delayed hydration of anhydrous binder particle available. This is likely to provide huge benefits in terms of durability also in the cracked state [23–25], which, as a matter of fact, is the ordinary service-life condition of concrete structures already at SLS [26–30].

In this context, the identification of the stress–strain law in direct tension of HPFRC and UHPFRC mixes is of utmost importance, and a few approaches can be found in the literature [31–37], despite the difficulties linked to the inherent redundancy of the most common adopted indirect tension tests (see also [38]). As it is well-know, in fact, the stress-redistribution taking place in a section subjected to bending makes it difficult the identification of key parameters such as first cracking stress or localization stress.

In the present paper, the approach adopted for the characterization of the tensile constitutive behaviour of three HPFRCs and for the identification of the main mechanical parameters is described, based on an inverse-analysis procedure applied to 4-Point Bending Test (4PBT) on small beams. The outcome is then compared with the results of Double Edge-Wedge Splitting (DEWS) tests [39]. Such procedure has been implemented with the final aim of assessing the effect brought in by two types of fibres and cement.

Three different HPFRC mixes have been studied, using straight steel or amorphous metallic fibres, and CEM I or CEM III cement types. In this regard, it is worth noting as CEM III has been attracting more and more attention in the last years [40–43] because of the lower content of Portland Cement (thanks to its partial replacement with slag), this being advantageous in the view of concrete sustainability. CEM III also lead to denser cement matrix and lower permeability, to the advantage of concrete durability, even in very aggressive environments [44, 45].

Within the framework of increased sustainability, also amorphous metallic fibres are showing interesting properties in terms of both mechanical performance [46–48] and sustainability [49–54], thanks to the lower energy consumption and CO_2-emissions required in the production phase with respect to conventional deformed steel fibres [54]. Furthermore, the production process based on rapid cooling down of molten metal brings to a microstructure based on irregular arrays of atoms which leads to a lower specific gravity and very high corrosion resistance, even higher than stainless steel fibres [55]. The excellent mechanical performance reported in the literature, however, can be jeopardized by the hydrophobic behaviour of the surface of amorphous alloy fibres [56], which may lead to poor mechanical performance of the cement paste surrounding the fibres [57, 58].

In the following, the three investigated mixes have been studied in terms of tensile mechanical response specifically addressing the effects brought in by the introduction of amorphous metallic fibres and the replacement of cement type CEM I with CEM III. The parallel study on their durability-related self-healing performance can be found in [59].

2 Program of the experimental investigation

2.1 HPFRCs design and mixing protocol

Three different HPFRC mixes have been designed in order to investigate the effects of cement and fibre types on the tensile mechanical response in terms of first cracking and peak strength, ductility and cracks pattern, as detailed in the following. In Table 1, where the proportions of all mixes are reported, it can be seen as the reference HPFRC (mix XA-CA) contains 1100 kg/m^3 of binder, namely 600 kg/m^3 of cement type CEM I 52.5R and 500 kg/m^3 of ground granulated blast furnace slag, mixed with 982 kg/m^3 of silico-calcareous sand (maximum size of 2 mm) and 1.5% by volume of straight steel fibres. The water to cement and water to binder ratios are 0.33 and 0.18, respectively, while the binder/sand/water volume fractions approach the proportion 2:2:1.

Regarding the other two mixes, in the first one, steel fibres have been replaced with metallic amorphous fibres in the same volume fraction (mix XA-CA-Amf), while in the second one, CEM I has been replaced with CEM III (mix XA-CA-CEMIII). Straight steel fibres are characterized by a length $l_f = 20$ mm and a diameter $d_f = 0.22$ mm (aspect ratio $\lambda_f = 91$ and single-fibre volume $\upsilon_f = 0.76$ mm^3), while amorphous fibre by a length $l_f = 15$ mm, a width $w_f = 1$ mm and a thickness $t_f = 0.024$ mm (equivalent diameter $d_{eq} = 0.18$ mm, aspect ratio $\lambda_f = 86$ and single-fibre volume $\upsilon_f = 0.36$ mm^3). It can be observed that the aspect ratio of the two fibre types is rather similar (100 and 86), while single-fibre volume is very different (0.76 and 0.36 mm^3) this leading to a larger number of fibres for a given fibre-to-concrete volume fraction in the case of amorphous metallic type.

The mixing protocol consisted in mixing the solid parts, adding 200 l/m^3 of water together with the superplasticizer. Crystalline admixture Penetron Admix® has been also introduced in the content of 4.8 kg/m^3 (0.8% by cement mass) as a stimulator of the autogenous healing capacity [59, 60].

In Table 1, compressive strength measured on 100 mm-side cubes at the reference time t_0 (= 90 days after casting = beginning of testing campaign) is reported. The mix with amorphous fibre proved a decrease of about 20% with respect to the two mixes with steel fibre, probably due to the combination of two detrimental aspects:

- higher flaw-effect brought in by fibres in the former case due to the almost 2-times higher number of fibres per unit volume of concrete and to the nearly 5-times higher specific lateral surface;

Table 1 Mix composition of the investigated HPFRCs

Constituents	XA-CA		XA-CA-Amf		XA-CA-CEMIII	
	[kg/m^3]	[% by vol]	[kg/m^3]	[% by vol]	[kg/m^3]	[% by vol]
CEM I 52.5	600	19.5	600	19.5	–	–
CEM III 52.5	–	–	–	–	600	19.5
Slag	500	17.5	500	17.5	500	17.5
Water	200	20.0	200	20.0	200	20.0
Steel fibres	120	1.5	–	–	120	1.5
Amorphous fibres	–	–	111	1.5	–	–
Sand (0–2 mm)	982	38.0	982	38.0	982	38.0
Superplasticizer	33	3.3	33	3.3	33	3.3
Crystalline adm	4.8	0.2	4.8	0.2	4.8	0.2
$f_{cm,cubes}$ [MPa]*	137		107		136	

Straight steel fibres

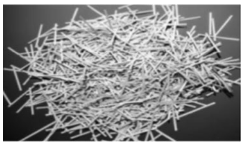

Amorphous metallic fibres

*Compressive strength on 100 mm-side cubes at time t_0 (= 90 days after casting = beginning of testing campaign)

- the hydrophobic behaviour of the surface of amorphous alloy fibres [56], which may leads to poor mechanical performance of the cement paste surrounding the fibres and thus to a decrease of the compressive strength, as also observed in [57, 58].

2.2 Test setups and specimen geometries

The mechanical characterization has been performed via 4-Point Bending Tests (4PBT) on un-notched small beams, with two different geometries described in the following. 4PBT on un-notched specimens is preferred (with respect to 3PBT on notched prisms) in order to investigate multiple cracking in the constant-moment central region (L_o in Fig. 1). During the test, both the vertical deflection and the Crack-Opening Displacement—COD across the central region of the specimen have been monitored via two LVDTs each (see Fig. 1).

Vertical LVDTs have been mounted on an aluminium frame simply supported on the specimens itself in correspondence of the two supports, while horizontal LVDTs have been fixed to metal platelets directly glued to the specimens. Tests have been performed in stroke-displacement control at 90 days after casting ($=t_0$), in order to allow the major part of long-term cementitious/pozzolanic reactions in cement and slag to be concluded.

Most of the 4PBTs have been performed under monotonic loading (thus constantly increasing the stroke displacement), while a few have undergone unloading-loading cycles so to investigate the variation of the unloading/loading stiffness for increasing values of the total deflection and crack opening as well. In the following, the former type is called *monotonic test* and the latter is referred to as *cyclic test*.

For each mix, six $100\times100\times500\text{mm}^3$ specimens (referred to as *deep beams* in the following) and twelve $100\times25\times500\text{mm}^3$ specimens (referred to as *thin beams* in the following) have been tested. For both geometries, the span over thickness ratio is larger than 4, thus they can be both considered as slender beams, thus allowing the plane-section assumption.

Deep beams have been cast in individual plastic moulds, while thin slabs ($1000\times500\times25\text{mm}^3$) have been cast and then cut to obtain the *thin beams* (see Fig. 1a). After cast, all specimens were stored in climate chamber (R.H. = 90%, T = 20 °C) until testing (thus for 90 days).

It is worth noting that the production process has some important effects on the mechanical response considering that, in the case of thin slabs, the casting procedure fostered the alignment of the flow of the fresh self-consolidating mix along the longer side (see Fig. 1a). Since *thin beam* specimens have been cut with their longitudinal axis parallel to the flow of concrete, a sizable better alignment of the fibre is expected if compared to that of *deep beams* (as also investigated in [61]), with peak stress in bending up to 50% higher in the former case.

After bending tests have been performed on *thin beams*, specimens for Double-Edge Wedge Splitting test (DEWS) have been obtained by cutting the two 100 mm ends, thus obtaining $100\times100\times25\text{mm}^3$ specimens. The ligament cross-sections of the DEWS specimens are defined by cutting grooves and notches

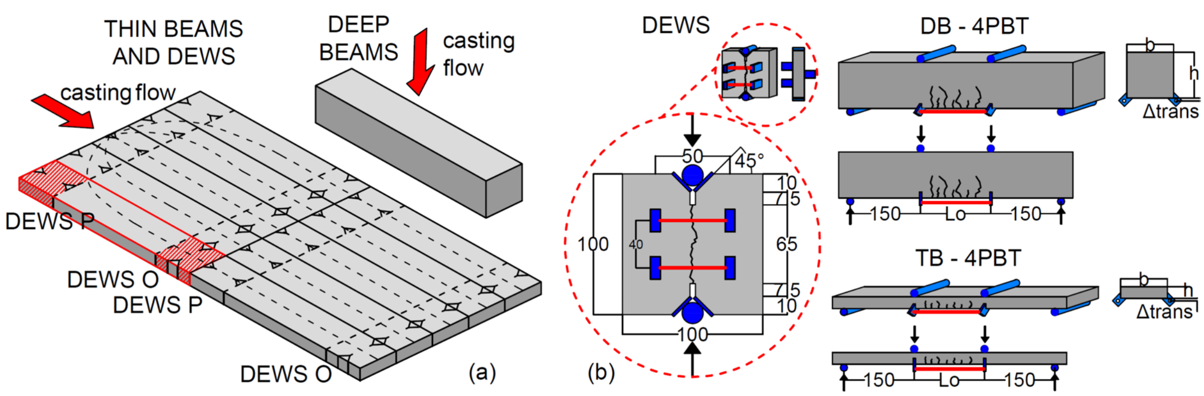

Fig. 1 **a** Scheme for specimens' production and **b** DEWS and 4PBT dimensions (in mm)

in the square tile specimens via a water-cooled diamond blade (see Fig. 1a).

DEWS samples have been cut in order to have half of the specimens with the ligament orthogonal (DEWS O) or parallel (DEWS P) to the aforementioned alignment of the fibres, in order to be able to identify a lower and upper bound for the tensile constitutive response. It is worth noting as the comprehensive experimental and numerical investigation reported in [39] comparing the results of flexural test and DEWS, proved as DEWS allows to reliably and straight forwardly identify the overall uniaxial tensile behaviour of HPFRC mixes (very similar to the ones herein presented).

2.3 Experimental plan

The first step of the experimental campaign is represented by the mechanical characterization in tension of the three mixes at the reference time ($t_0 = 90$ days after casting). In particular, for each mix, the six *deep beams* have been tested in 4PBT at time t_0, in order to define the reference stress–deflection response. Based on these results, the inverse analysis described in the following has been performed to calibrate the reference constitutive behaviour in direct tension at time t_0.

Six out of twelve *thin beams* per mix have been tested at time t_0 also, so to evaluate the effect on the flexural response brought in by the different production process and by the different geometry thanks to the comparison with the results related to *deep beams*.

It is worth noting that the characterization on thin beams has been performed addressing a specific structural application, namely one of the demonstrators for the ReSHEALience project, consisting in a geothermal water tank made with precast 30 mm-thick slabs [4, 62, 63]. In order to assess the possible detrimental effect associated to the immersion in geothermal water, and the subsequent sulphate/chloride attack, six *thin beams* have been tested after additional six months ($t_0 + 180$ days), three beams after having been kept under immersion in geothermal water for 6 months and three under immersion in tap water for 6 months.

As said above, at time t_0, after flexural tests on six *thin beams*, twelve DEWS specimens have been cut, six with fibres parallel (DEWS P) and six with fibres orthogonal (DEWS O) to the ligament (which is the expected fracture plane during DEWS test). This enabled to evaluate a rather good approximation of the lower and upper bounds of the behaviour in direct tension of the mixes under investigation. As abovementioned, in fact, it has been proved in [39] as DEWS yields a good estimation of the effective behaviour in direct tension. In Table 2 the tests plan of each mix is summarized.

3 Identification of the tensile consitutive law

3.1 Indirect tension test and stress redistribution

As it is well known, the great benefits brought in by fibres in (UHP)FRC can be highly effective both in direct tension (truss structures), and in 1D or 2D bending (as in the case of beams and slabs, respectively). Moving from direct tension, in which any point of the structural element experiences the same stress-state (hence, no stress-redistribution can take place), to 1D and, even more, to 2D bending, where stress-redistribution can occur at a sectional level (in the former case) or at a structural level (in the latter one), the overall ductility increases. As clearly described in [38], this allows that structures made of materials which show softening behaviour in direct tension can even exhibit a hardening behaviour in bending.

As mentioned in the introduction, direct tension tests are rarely performed due to their complexity in implementation, thus making flexural tests (3PBT or 4PBT) commonly preferred. Hence, it is clear that the characterization of cementitious materials in

Table 2 Testing plan

Time t_0	6 tests in 4 PB on *deep beams*	6 tests in 4 PB on *thin beams*	12 DEWS tests
$t_0 + 180$ days	3 tests in 4 PB on *thin beams* after 6 months under immersion in tap water	3 tests in 4 PB on *thin beams* after 6 months under immersion in geothermal water	

direct tension is not trivial, due to the need of inverse analysis procedures. Generally speaking, the possible approximation introduced by such inverse-analysis is satisfactory considering that the most common applications for cementitious materials regard structural elements subjected to bending. It is worth noting, anyway, that these new advanced materials have been used in the recent decades in other structural applications involving direct tension, such as truss structures [64], column jacketing [65] and beam retrofit [66].

In Fig. 2, the typical behaviour in direct tension and in bending in case of strain-hardening materials is schematically reported. Three different stages can be detected: (1) initial perfect elastic branch ended by the formation of the first crack at $\sigma = f_t$ (green curve), (2) hardening branch in which the formation of multiple cracks can be observed (red curve), and (3) softening behaviour due to the localization of the deformation in one single crack (black curve, starting from $\sigma = f_{tuc}$ in direct tension and $\sigma = f_{tu,b}$ in bending, with $f_{tu,b} > f_{tuc}$). Hardening behaviour in stage (2) can be observed just if the amount of fibre allows for increasing the external load after first crack is formed thanks to the bridging-effect of fibres crossing the cracks. The minimum quantity of fibres needed for providing hardening behaviour decreases moving from direct tension to 1D and to 2D bending.

In is worth noting to recal that in Fig. 2 (as well as in Figs. 5, 6, 7, 8, 9), the stress is referred to as σ for direct tension only, since the calculated stress ($\sigma = N/A$) correspond to the effective stress in the cross-section. On the other hand, in the case of bending, the stress is referred to as nominal (or conventional) stress σ_n, since it is calculated assuming a linear stress profile ($\sigma_n = M/W$) as conventionally performed (see also [38]), thus losing the correspondence to the effective stress distribution in the cross-section.

3.2 Indirect tension tests and inverse analysis

The characterization in tension of a cementitious material requires the identification, in particular, of f_t and f_{tuc} (and of the correspondent strains), since they define the multiple cracking stage. When mechanical characterization is performed via indirect tension tests such as bending, however, the identification of such parameters is made difficult by the rather smooth transition among the elastic, the hardening and the softening branches, due to the stress redistribution across the specimen depth. This is the reason why inverse analysis must be implemented.

In the present study, such procedure has been implemented on 4PBTs, based on the approach developed at Universitat Politècnica de València (UPV), called *simplified 4-Point Inverse Analysis with softening correction method* (4P-IA) [34–36]. Such approach has been developed and validated on a wide dataset of 4PBTs in small beams with dimensions $100 \times 100 \times 500$ mm^2 (see Fig. 3a).

The method is based on the assumption of a simplified trilinear curve for the constitutive law in tension, identified by the following parameters (see Fig. 3b): elastic modulus (E), unloading modulus (E^*), tensile strength (f_t), ultimate tensile strength (f_{tu} *or* f_{tuc}) and its associated strain (ε_{tu}), crack opening at the intersection of the line that defines the initial slope of the crack-opening (w) descending branch to the w axis (namely, w_0). A softening correction f_{tuc} of the f_{tu} parameter obtained from the 4P-IA [35] is adopted in the case of HPFRC and UHPFRC that exhibits strain-softening tensile behaviour ($f_{tu} \leq f_t$, with yields $f_{tuc} = f_{tu}$ in the strain-hardening case) [35]. Those parameters are defined based on 4 given key points identified in the experimental 4PBT curve (see Fig. 3c).

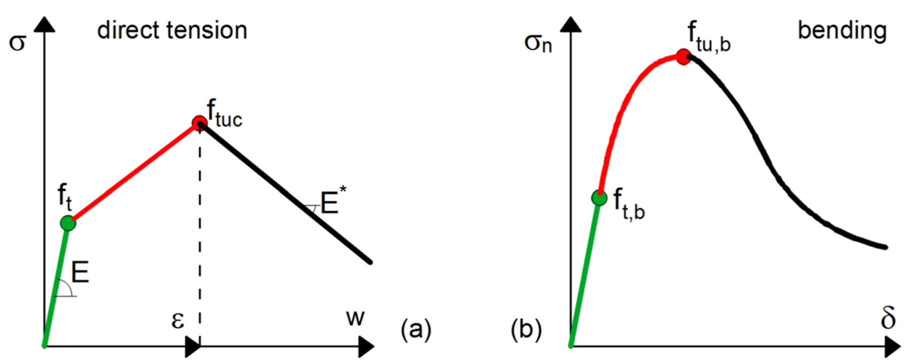

Fig. 2 Schemes of (**a**) $\sigma - w$ curves in tension and (**b**) $\sigma_n - \delta$ curves in bending

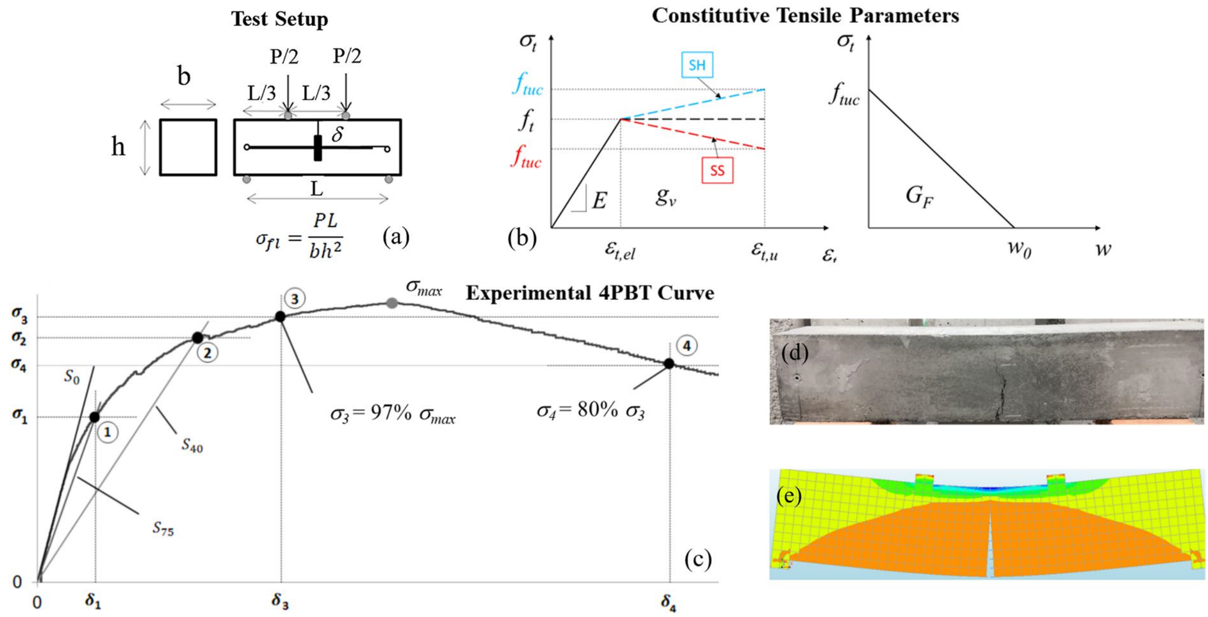

Fig. 3 Typical setup for 4PBT on small beams (**a**), tensile constitutive law approximated by a trilinear curve (**b**), 4 key points in the experimental $\sigma - \delta$ curve under 4PBT for the application of 4P-IA (**c**), and comparison between a specimen at the end of 4 PB testing (**d**) and its Non-Linear FEM simulation (**e**)

The calibrated constitutive laws in direct tension have been then used for "back" simulating the 4PBTs via both numerical and analytical calculations. For the latter, a method based on closed-form formulations of moment–curvature relationships has been used, namely the so-called *Hinge Model* [34–36], where the conversion of the theoretical strain into the experimental COD is performed with reference to the LVDT gauge length under the assumption of constant curvature (being the bending moment constant). This translates into the assumption of a non-linear hinge in the multiple-cracking region. Outside the central constant-moment region, elastic behaviour is assumed.

On the other hand, for the non-linear numerical analyses, Diana finite element package [67] has been used, by adopting a discrete cracking approach. According to this method, the constitutive law for HPFRC/UHPFRC in the post-localization regime (hence, in the σ-w domain) is implemented as interface behaviour at mid-span section where a discrete crack is a priori defined, while the rest of the specimen is modelled by a smeared cracking approach following the constitutive law for HPFRC/UHPFRC in the pre-localization regime (hence, in the σ-ε domain). According to this modelling assumption, the discrete crack is activated just when crack localization takes place, thus effectively simulating the real behaviour observed during the experimental tests. On the other hand, for tensile strains lower than ε_{tu}, the whole specimen behaves just according to the smeared crack approach. In Fig. 3d, e, the comparison is reported between an experimental test and the simulation carried out via Diana software.

4 Results and discussion

4.1 Experimental tests at time t_0

The average values of the peak stresses observed at the reference time t_0 in 4PBT (on *deep beams*—DB and *thin beams*—TB), $f_{tu,b}$, and DEWS O, f_{tu}, are reported in Table 3 and in Fig. 4a, b. In Table 3 and Fig. 4a, b, it is reported also the outcome in terms of mechanical parameters evaluated via the inverse analyses on *deep beams*—DB (namely, elastic modulus E, tensile strength f_t, ultimate tensile strength f_{tu}, ultimate tensile strain ε_{tu} and maximum crack-opening w_0). The typical crack pattern observed in *deep*

Table 3 Average values of the mechanical parameters from indirect tests and inverse analyses

Mix	Experimental tests at time t_0				Inverse analysis at time t_0				
	4 PB	4 PB-DB	4 PB-TB	DEWS O	4P-IA on 4 PB-DB				
	crack sp. [mm]	$f_{tu,b}$ [MPa]	$f_{tu,b}$ [MPa]	f_{tu} [MPa]	E [GPa]	f_t [MPa]	f_{tuc} [MPa]	ε_{tu} [MPa]	w_0 [mm]
XA-CA	23	16.78	25.31	7.95	45.05	8.04	6.67	2.90	2.58
XA-CA-Amf	27	19.04	20.85	8.70	46.34	8.57	8.86	1.44	0.97
XA-CA-CEM III	21	20.19	25.10	8.00	47.65	8.02	8.39	3.47	2.58

(4 PB = 4-Point Bending; DB = *deep beams*; TB = *thin beams*; crack sp. = average crack spacing evaluated on DB and TB)

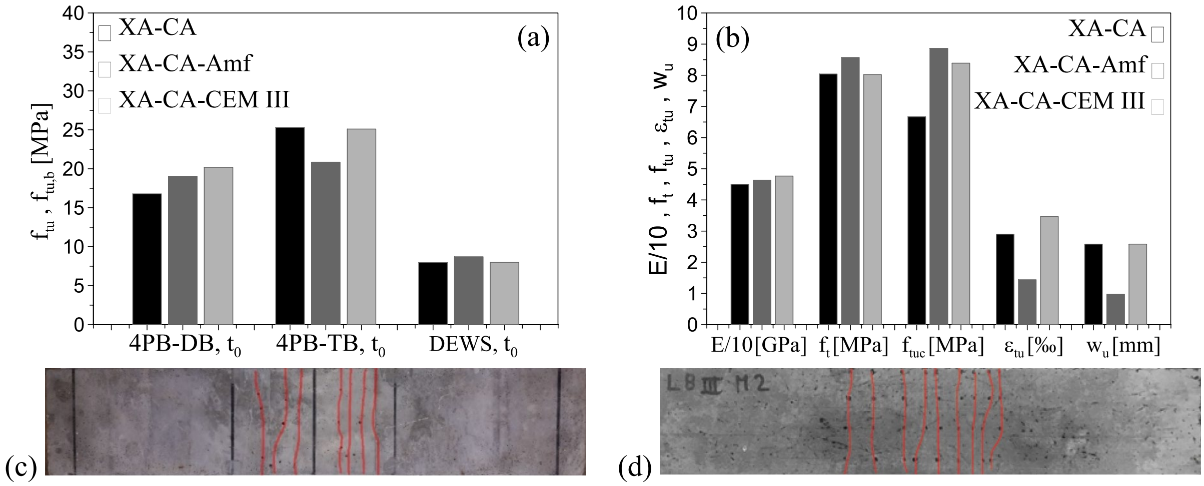

Fig. 4 Mechanical parameters from experimental tests (**a**) and inverse analyses (**b**) (see also Table 3), and typical crack patterns in 4PBT before crack localization for *deep beams* (**c**) and *thin beams* (**d**)

beams and *thin beams* before crack localization is also shown (Fig. 4c, d).

In Fig. 5, the results from 4PBT are reported in terms of $\sigma - \delta$ curves, where δ is the vertical mid-span displacement and σ_n is the nominal stress evaluated as $\sigma_n = P\ L\ /\ (b\ h^2)$, being P the total applied load, L the test span and b, h specimen width and thickness. It can be observed that the scattering among the curves of the same mix is quite typical for flexural tests because of the differences in terms of fibre arrangement among the specimens and inherent heterogeneities of cementitious composites.

The average peak stress in bending on *deep beams*, $f_{tu,b}$, is equal to 17, 19 and 20 MPa for mixes XA-CA, XA-CA-Amf and XA-CA-CEMIII, respectively (see Table 3), while it ranges from 21 to 25 MPa for *thin beams*. The two mixes with steel fibres, namely XA-CA and XA-CA-CEMIII, were expected to yield very similar peak stresses, since fibre dosage and typology is the same. This is consistent with the experimental evidence, and the lower value experienced by XA-CA can be ascribed to the higher scattering.

On the opposite, it is worth noting as mix XA-CA-Amf also provides very similar peak stresses (at least regarding *deep beams*), nevertheless the amorphous metallic fibres are very different in terms of physico-mechanical properties, geometry and surficial features.

The most remarkable difference in the response of the three mixes consists in the post-localization phase, since mixes with steel fibres show higher ductility with a smoother softening branch for both *deep beams* and *thin beams*. This aspect is well confirmed by the parameters evaluated via 4-Point Inverse Analysis, in which the ultimate strain (before localization)

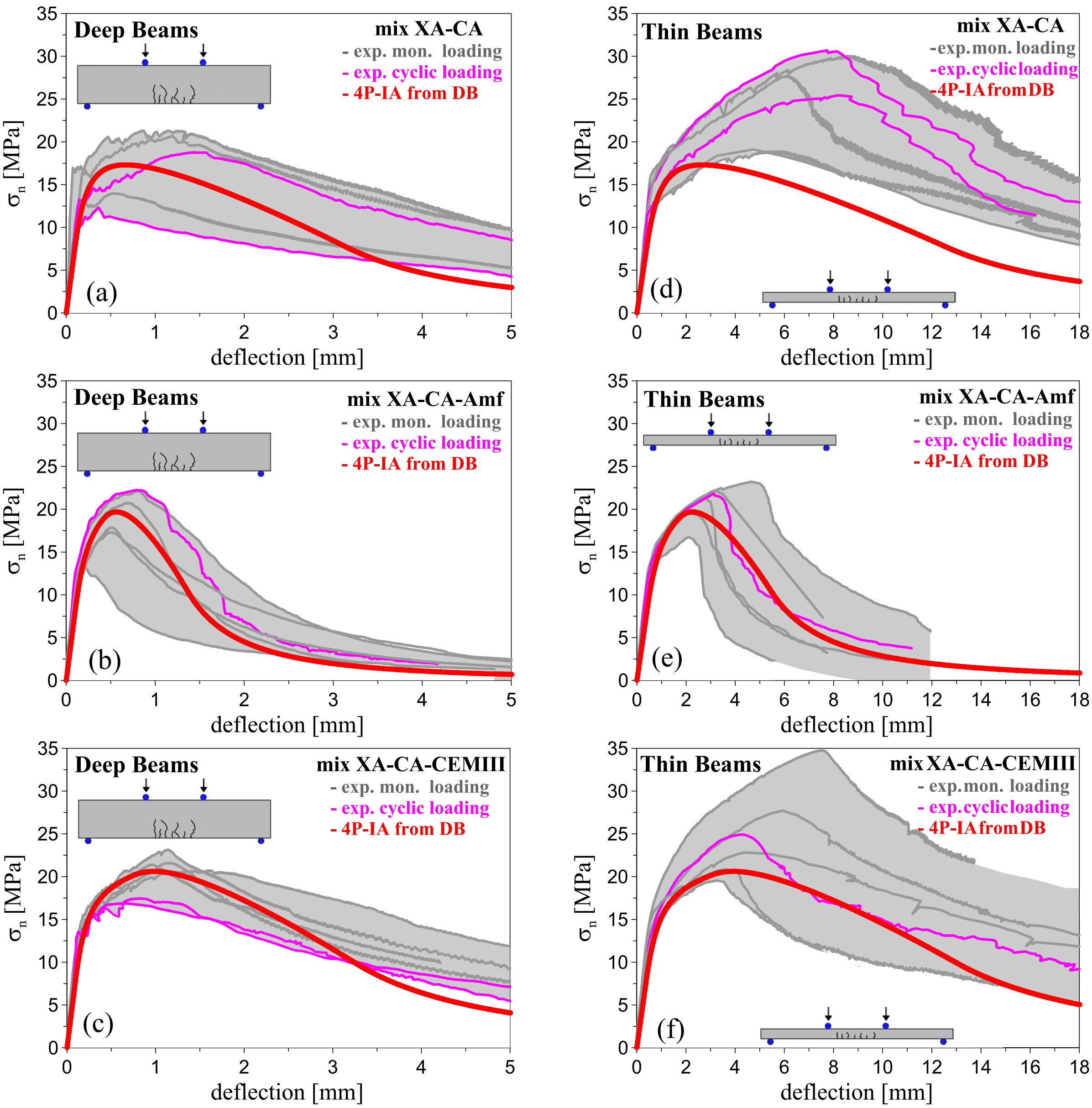

Fig. 5 Plots of $\sigma - \delta$ curves from 4PBT on *deep beams* (**a**–**c**) and on *thin beams* (**d**–**f**) for XA-CA (**a**, **d**), XA-CA-Amf (**b**, **e**) and XA-CA-CEMIII (**c**, **f**) (In magenta colour the experimental envelope of the cyclic loading curves)

of mixes XA-CA and XA-CA-CEM III is more than double the one of mix XA-CA-Amf, while the ultimate crack width of the formers is more than 2.6 times larger than the one of the latter.

Such outcome can be ascribed to three major aspects. Firstly, the larger specific lateral surface of amorphous fibres with respect to steel ones leads to a stiffer bond-slip response at fibre-matrix interface [68]. Secondly, it has been reported in [46, 47, 68] that the failure in tension of amorphous fibres can be observed at the cracked surface (this being possibly a consequence of the stiffer fibre-matrix bond). Finally, the hydrophobic behaviour of the surface of amorphous alloy fibres [56] which may leads to a more brittle response at the fibre-matrix interface.

These features lead to a narrower multiple-cracking phase in the constitutive law and a more pronounced softening response after localization. This is reflected also by the average spacing between adjacent cracks (measured in all 4-point flexural tests in the central region where the bending moment is constant), which is smaller in case of steel fibres (21–23 mm) rather than in the case of amorphous ones (27 mm), as reported in Table 3.

The increased ductility provided by steel fibres can be observed also by comparing the results from tests on *deep beams* and *thin beams*. In mixes XA-CA and XA-CA-CEM III, the peak stress increases of 51% and 24%, respectively, while in mix XA-CA-Amf the increase is limited to 10%, due to the higher sectional redistribution capability of stresses allowed by steel fibres. Such difference can be also likely ascribed to a less effective alignment of amorphous fibres with pouring direction in the production of thin beams, this being, together with the scale effect [69], a major reason for the higher flexural strength observed with respect to *deep beams*.

Another interesting aspect can be emphasized looking at Fig. 6, where the results regarding 4PBT with unloading-loading cycles (called in the following "cyclic loading") are reported.

In particular, it can be noticed as unloading-loading cycles proves to be rather stable in mixes XA-CA and XA-CA-CEM III for increasing values of vertical displacement δ, while in mix XA-CA-Amf they show a visible reduction of the slope, this being an indication of a variation in the performance of fibre-matrix interaction (due to fibre and/or bond failure). On the opposite, the overall response in bending appeared to be not affected by cyclic loading more than by monotonic loading for all the three mixes, as it can be observed in Fig. 5, where the grey results refer to monotonic loading and the magenta curves to cyclic loading.

4.2 Inverse analysis and numerical/analytical simulations at time t_0

As described in previous sections, inverse analysis has been performed on 4PBT on *deep beams* according to the simplified 4-Point Inverse Analysis with softening correction method (4P-IA), and the obtained parameters are presented in Table 3. The procedure has been implemented on the results on *deep beams* only (thus excluding the tests on *thin beams*), since 4P-IA has been validated for such specific geometry [34–36]. The constitutive laws in tension estimated via inverse analysis are reported in Fig. 7 in terms of stress–strain curves, σ-ε, and stress-crack opening curves, *σ*-*w*, in the pre- and post-localization stage, respectively (in black colour for each single specimen, and in red colour for the average curve of each mix). The comparison among the three investigated HPFRCs highlights that all of them show an almost plastic behaviour in tension (slightly softening for mix XA-CA and slightly hardening for mixes XA-CA-Amf and XA-CA-CEMIII), with a strain-at-localization around 2.9–3.5‰ for the mixes with steel fibre and about 1.4‰ for the mix with amorphous fibre.

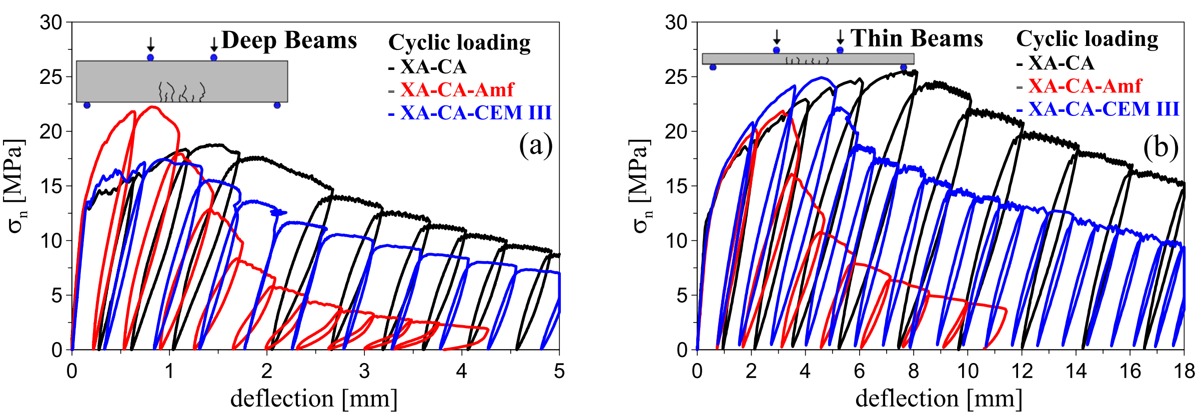

Fig. 6 Plots of $\sigma - \delta$ curves from 4PBT under cyclic loading on *deep beams* (**a**) and *thin beams* (**b**) for XA-CA, XA-XA-Amf and XA-CA-CEMIII

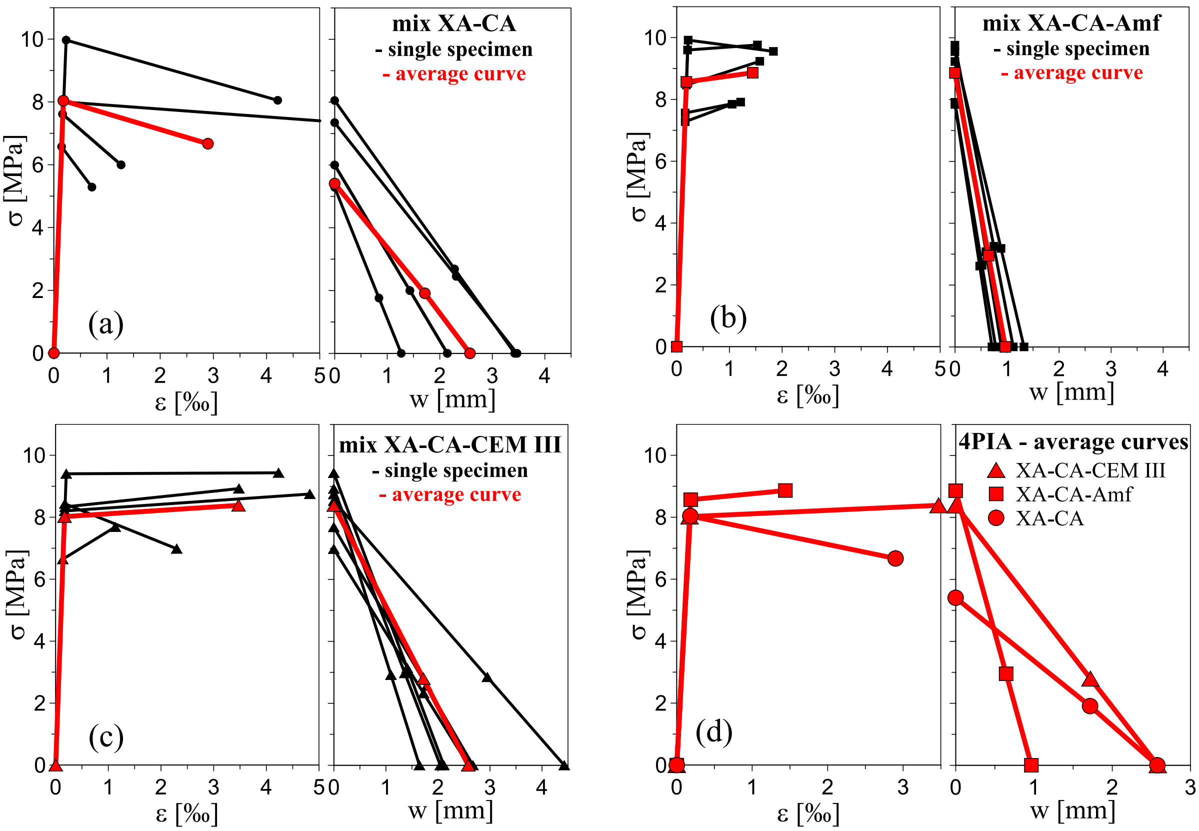

Fig. 7 Plots of $\sigma - \varepsilon$ and $\sigma - w$ curves in direct tension (inverse analysis) for XA-CA (**a**), XA-CA-Amf (**b**) and XA-CA-CEMIII (**c**), and comparison of the average curves of the 3 mixes (**d**)

It is worth noting that, also in the case of strain-softening, the response between the attainment of f_t, with the formation of the first cracks, and f_{tuc} can be described in σ-ε domain (instead of σ-w domain), because it can be still considered as a microcracking phase. Macrocrack localization only starts to develop when f_{tuc} level is reached, since the corresponding equivalent deformation (strain) ε_{tu} represents the condition in which fibre efficiency is maximum on average and debonding process has reached fibre end on average (as also happens in strain hardening). This is consistent with the observed average crack spacing of 21–27 mm reported in Table 3, which is compatible with microcracking.

The constitutive laws obtained via inverse analyses are also compared in Fig. 8 with the experimental results yielded by the DEWS tests, in terms of σ – *COD* curves. In the plots, *COD* is the crack opening displacement measured by the LVDTs placed across the main crack with a base length of 50 mm, while σ_n is the nominal stress evaluated as $\sigma_n = \alpha\, P/(t_{lig}\, h_{lig})$, being α the coefficient taking into account the inclination of the notch and the *loading blade-to-specimen* friction (with $\alpha = 0.89$ for the adopted setup [39]), P the total applied load and t_{lig}, h_{lig} the thickness and the height of the ligament.

It is worth recalling that 4PBT Inverse Analysis is based on a "hinge model", which is technically a simplified approach to reproduce the behaviour of un-notched prismatic specimens. Based on this model, it was derived a simplified procedure to estimate the tensile response of the material in the flexural loading versus deflection behaviour of un-notched prismatic specimens (4P IA). 4P-IA has been validated in the presented form only in the case of *deep beams*. Thus, the presented comparison with *thin beams* (TB) or DEWS do not assume to consider that the fundamentals of the methodology

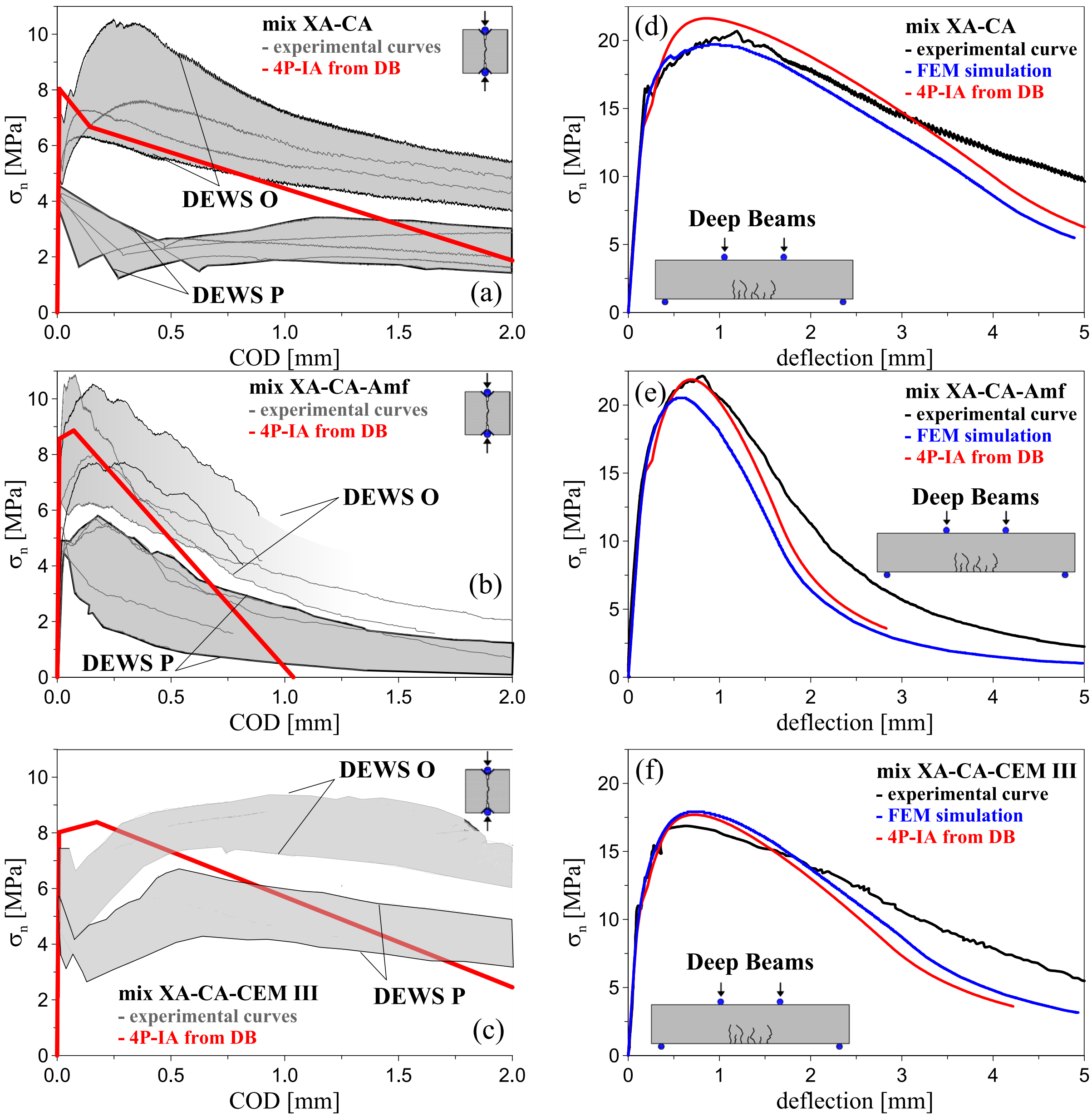

Fig. 8 Plots of σ – COD curves from DEWS for **a** XA-CA, **b** XA-XA-Amf and **c** XA-CA-CEMIII and **d**–**f** comparison among one experimental curve in 4 PB on *deep beam* and the correspondent analytical/numerical curves obtained via Hinge Model and FEM simulations

are the same but represent a first attempt to cross-compare the results.

Furthermore, in comparing the experimental results of DEWS with the tensile law obtained by applying 4P-IA to 4PBT on *deep beams*, two main aspects must be recalled. First of all, constitutive laws are expected to be closer to DEWS O, in which fibres are orthogonal to the ligament, so effectively activating their crack-bridging capability, while in DEWS P the matrix alone response is almost observed, since fibre are just negligibly working. Secondly, as already mentioned for the case of *thin beams*, the better fibre alignment fostered by their production procedure (with respect to *deep beams*) brings to a higher peak stress and a more pronounced ductility. Despite these two aspects, the consistency between the results of the DEWS O and the integration of the constitutive laws obtained via 4P-IA is satisfactory.

A higher gap can be observed for mix XA-CA-CEMIII probably due to a less effective alignment of the fibres in the DEWS specimens, this higher dispersion resulting in a lower peak stress (compared to mix XA-CA) and in a far lower gap between the tests with fibres orthogonal or parallel to the load (DEWS O versus DEWS P). This hypothesis was corroborated by the visual inspection of the cracked surface of DEWS specimens after testing.

Regarding, in particular, mixes XA-CA and XA-CA-Amf for which the agreement proves to be very good, the integration of the 4P-IA is representative of the behaviour in direct tension. The steep slope of the softening branch obtained via 4P-IA curves can be ascribed to the fact that, as above mentioned, they were calibrated on the base of 4PBT on *deep beams*, where the worse alignment of the fibres with respect to thin beams and DEWS O, yields to a lower ductility in tension. Such preliminary, but very promising, comparison and cross validation between the results of 4P-IA performed on 4PBTs and DEWS will be the basis for future more systematic investigations built on a larger data set.

Considering the overall consistency of experimental results and inverse analyses, it is clear that, similarly to flexural tests, steel and amorphous fibres lead to comparable values of peak stress in direct tension (all comprised in the range 8–9 MPa), but markedly higher ductility is guaranteed by steel fibres with a higher value of strain at localization ε_{tu} (2.9–3.5‰ for XA-CA and XA-CA-CEMIII against 1.4‰ of XA-CA-Amf) and a less steep post-localization behaviour. Guaranteeing a strain at localization higher than 2.1–2.5‰ (namely the strain at yielding for commonly used steel reinforcement bars) is advantageous for the durability performance of fibre-reinforced concrete structures, since crack opening at SLS can be maintained within the limits provided by the standards also if the yielding of the rebars is attained.

Finally, as a further confirmation of the overall consistency in the results, the constitutive laws obtained via 4P-IA have been considered as input for simulating the bending tests via both the Hinge Model and FEM analyses. In Fig. 8d–f the comparison among experiments (on which 4P-IA was based) and analytical/numerical results is provided for one specimen per mix, showing a very good agreement which confirms the effectiveness of the inverse analysis procedure. For each of the three 4PBTs back simulated in Figs. 8d–f, the correspondent constitutive law derived from the same specimen has been used as input for the analytical/numerical simulation.

On the other hand, in Fig. 5, the results of the simulation of 4PBT on both *deep beams* and *thin beams* via the 1D analytical approach (Hinge Model) had been reported in red curves. For those simulations, the average values of the mechanical parameters evaluated via 4P-IA (red curves in Fig. 7d) have been used as input for each of the three mixes.

Comparing numerical and experimental curves in Fig. 5, it is worth noting, once again, as the effect of beam thickness is clearly evident in the tests, since a nominal peak stress generally 10–50% higher than in the case of *deep beams* is obtained from the tests on *thin beams*. This evidence can be ascribed to (1) the well-known scale-effect [69] and, to a major extent, to the above described (2) role played by beam production on fibre alignment. As highlighted in Sect. 2.2, the production procedure of *thin beams*, in fact, leads to a far better alignment of the fibre and improved response in bending, thus making not always recommended the adoption of a general law in tension for all specimen types (differing for both geometry, production process and consequent fibres orientation producing different fibres efficiency). This is the reason why the red curves of Fig. 5 represent a very good estimation for 4PBT in *deep beams*, while are closer to be a lower bound for *thin beams*. Despite this critical point, however, the overall consistency remains rather satisfactory, even more considering the simplicity of both the 4P-IA and the 1D analytical simulation (hinge model) implemented. This final evidence is very promising for the adoption of the described procedure to beam geometries different from the initial database on which the 4P-IA has been calibrated and validated (namely 4PBT on $100 \times 100 \times 500$ mm^3 specimens).

For the investigated mixes, performing 4PBT on "classical" $100 \times 100 \times 500$ mm^3 beams together with the implementation of 4P-IA proved to be representative also for rather different geometries (such as bending on *thin beams* or tension on DEWS) also if entailing different production procedures affecting fibre alignment, for which the recommended orientation factors have to be improved. Finally, it is worth noting as 4P-IA is conceived as a practitioner-friendly tool which, thanks to the choice of a trilinear approximation for the constitutive law in direct tension, can be considered as already Standards-oriented.

4.3 Experimental tests at time $t_0 + 180$ days

Considering the final application in the ReSHEALience project [4, 62, 63] for the three mixes herein investigated, a further experimental comparison has been carried out. For each mix, three *thin beams* have been tested in 4 PB after six months (at $t_0 + 180$ days) under immersion in geothermal water (where chlorides also were present) and other three nominally identical *thin beams* after six months (at $t_0 + 180$ days) under immersion in tap water. These tests have been carried out to assess the stability of the mechanical performance under the conditions the materials are expected to experience in the demonstrator of the project, consisting in a geothermal water tank.

In Table 4, the values of peak stress from 4PBT in thin beams, $f_{tu,b}$, for the reference condition at time t_0 and for the two curing conditions, have been shown together with their variation with respect to the reference (namely, the 4PBT on *thin beams* at time t_0 reported in Table 3 and in Fig. 5). In Fig. 9, the experimental curves are reported for the three mixes for the two curing conditions in grey colour, while the blue-shaded area represents the results of the 4PBT in thin beams in the reference conditions at time t_0.

The mix with amorphous alloy fibres featured a higher stability in aggressive environment, herein represented by the curing period of 6 months under immersion in geothermal water, as it can be observed comparing the peak stress after six months in tap or geothermal water (see Fig. 9 and Table 4). Mixes XA-CA and XA-CA-CEM III show a decrease of 23 and 11%, respectively, while mix XA-CA-Amf even reports an increase of 9%.

The better performance provided by XA-CA-Amf is likely made possible by the high corrosion resistance provided by the microstructure of amorphous fibres, as already reported in the literature [44–56]. On the opposite, in the case of steel fibres (mixes XA-CA and XA-CA-CEMIII), the superficial corrosion of the fibres, even though not sufficient to jeopardize their strength, may induce a decay of the fibre-matrix pull-out force, with the consequent loss in terms of overall flexural performance of the mixes [70, 71].

It is, however, interesting to observe that, as expected, bending strength increases moving from time t_0 to time $t_0 + 180$ days in tap water for mixes XA-CA and XA-CA-CEM III (in the extent of 26 and 30%, respectively) thanks to the improved fibre-matrix bond allowed by the delayed hydration process rightly favoured by the continuous presence of water [70, 72, 73]. On the other hand, for mix XA-CA-Amf, peak stress is almost constant in time, probably due to a different fibre-matrix interaction.

For steel fibre, in fact, fibre-matrix failure is driven by bond, while in case of amorphous fibre the interaction is probably driven by fibre collapse (as can be also argued in [68]), this explaining why the improvement in fibre-matrix bond allowed by 6 months water curing seems not bringing in any advantage in case of the mix with amorphous fibres.

Inverse analysis has not been performed in this case, since tests on *deep beams* have not been carried out. However, comparing grey and blue shaded areas of Fig. 9, representing the reference tests at time

Table 4 Average values of the mechanical parameters from indirect tests and variation of $f_{tu,b}$ in bending depending on curing conditions

Mix	4 PB-TB t_0 $f_{tu,b}$ [MPa]	4 PB-TB $t_0 + 6$ T $f_{tu,b}$ [MPa]	4 PB-TB $t_0 + 6$G $f_{tu,b}$ [MPa]	$f_{tu,b}$ 4 PB-TB $t_0 + 6$ T / $f_{tu,b}$ 4 PB-TB t_0	$f_{tu,b}$ 4 PB-TB $t_0 + 6$G/$f_{tu,b}$ 4 PB-TB $t_0 + 6$ T
XA-CA	25.31	31.88	24.42	1.26	0.77
XA-CA-Amf	20.85	21.01	22.86	1.01	1.09
XA-CA-CEM III	25.10	32.59	28.91	1.30	0.89

(4 PB = 4-Point Bending; DB = *deep beams*; TB = *thin beams*; t_0 = time t_0; $t_0 + 6$ T = $t_0 + 180$ days in tap water; $t_0 + 6$G = $t_0 + 180$ days in geothermal water)

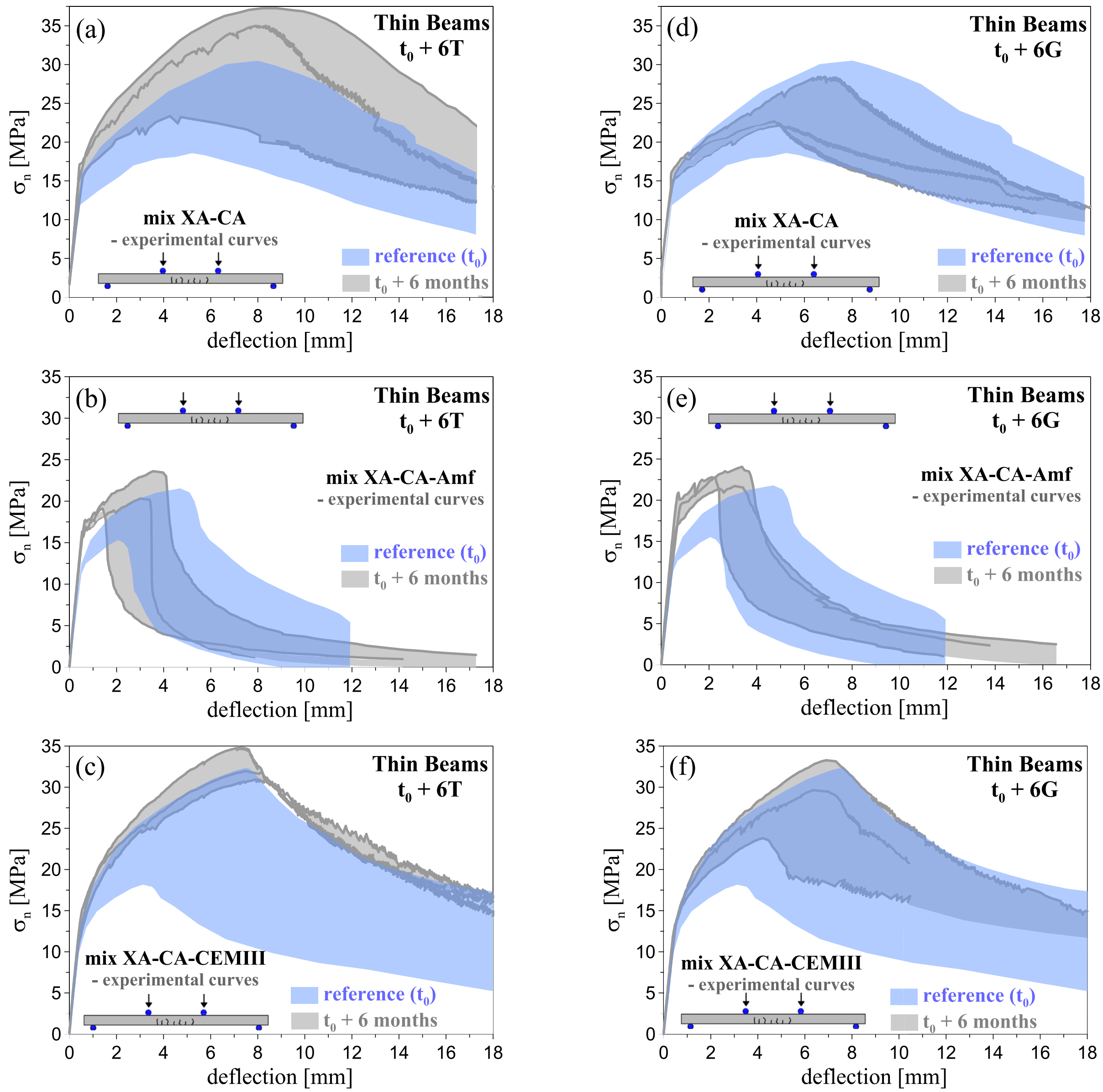

Fig. 9 Plots of $\sigma - \delta$ curves from 4PBT on *thin beams* after six months under immersion in tap water (**a**–**c**) and in geothermal water (**d**–**f**) for the three mixes, in grey colour, and results of 4PBT on *thin beams* at t_0 in blue-shaded areas (t_0 = time t_0; t_0 + 6T = t_0 + 180 days in tap water; t_0 + 6G = t_0 + 180 days in geothermal water)

t_0 and after 6 months curing, respectively, it can be observed that the main difference seems to consist in the flexural peak stress, while the shape of the post-localization stage appears the same, this suggesting that the variation in the flexural performance is meanly due to a variation in the ultimate tensile strength f_{tu} of the direct tensile response.

5 Concluding remarks

The study herein presented focuses on the mechanical characterization in tension of three High-Performance Fibre-Reinforced Concretes (HPFRCs) conceived for specific structural applications in extremely aggressive environments within the framework of the Research Project ReSHEALience (funded by the Horizon 2020 program).

The tensile characterization has been performed through a combined identification procedure based on experimental 4-Point Bending flexural tests and indirect tensile tests (Double Edge Wedge Splitting—DEWS) and the simplified 4-Point Inverse Analysis with softening correction method (4P-IA). The constitutive laws obtained from inverse analysis have been used as input for numerical/analytical analyses to back simulate bending tests on both thicker and thinner specimens (referred to as *deep beams* and *thin beams*, respectively) and on DEWS so to check the overall consistency of the approach.

The study focuses on three different HPFRC mixes, made of either CEM I or CEM III, containing 1.5% by volume of either straight steel fibres or amorphous metallic fibres. Based on the results obtained, the following conclusion can be summarized:

- The identification procedure confirms an almost perfect-plastic tensile constitutive response of the investigated mixes. In particular, the reference mix XA-CA, with CEM I and steel fibres, showed a slightly softening behaviour, while the mix with amorphous fibre (and CEM I) XA-CA-Amf and the mix with CEM III (and steel fibres) XA-CA-CEMIII both proved a slightly hardening response after first cracking.
- The two mixes with steel fibre yield a sizably higher value of strain-at-localization, this being around 2.9–3.5‰ according to the inverse analysis, while amorphous fibre leads to a more brittle response with a value of strain-at-localization close to 1.4‰. This outcome is rather relevant recalling as 2.1–2.5‰ represents the yield strain of ordinary steel, value of deformation which could be abundantly overpassed in the case of steel fibres, while amorphous fibres did not allow to reach such threshold. This aspect is very important at the Serviceability Limit State, since it guarantees that no crack-localization of concrete is attained at steel rebar-yielding, with the subsequent advantages for the optimization of reinforcement amount in terms of durability performance. The lower strain capacity allowed by amorphous fibre is probably caused by the stiffer and more brittle fibre-matrix bond and by the occurrence of fibre failure in correspondence of cracks, all aspects leading to a lower ductility in the overall response in tension of the fibre-reinforced concrete mix.
- The values of first cracking stress (f_t) and ultimate tensile strength (f_{tu}) in direct tension of the three mixes are rather similar, their average values being comprised in the range 8–9 MPa and 7–9 MPa, respectively.
- In the 6-month curing in tap water, the mixes with steel fibre showed a significant increase of the flexural capacity, probably thanks to the improvement of the fibre-matrix bond, while in the mix with amorphous fibre no significant variation has been observed. On the contrary, specimens cured for six months in geothermal water proved a non-negligible reduction in flexural capacity (with respect to curing in tap water) for the mixes with steel fibre, probably due to the degradation of fibre-matrix bond because of surface fibre corrosion, while no significant variation has been observed for the mix with amorphous fibres thanks to their very high resistance against corrosion.
- It is worth remarking the very similar response of the two mixes with steel fibres, proving the very good performance of CEM III which also has a lower environmental impact with respect to CEM I.

The promising mechanical response in tension provided by the three mixes together with the effectiveness in the identification of the main constitutive parameters via inverse analyses are the bases for the following step, namely the design of the full-scale demonstrators of the Project and the following validation of the developed procedure.

Acknowledgements The research activity reported in this paper has been performed in the framework of the ReSHEALience project (Rethinking coastal defence and Green-energy Service infrastructures through enHancEd-durAbiLity high-performance cement-based materials) which has received funding from the European Union's Horizon 2020 research and innovation program under grant agreement No 760824. The information and views set out in this publication do not necessarily reflect the official opinion of the European Commission. The authors acknowledge the cooperation of MEng. Lorenzo Papa, Stefano Passoni, Angelo Alferi, Nicola Borgioni, Andrea Cervini and Luca Famiani in performing experimental tests, in partial fulfilment of the requirements for the MEng in Civil Engineering and Building Engineering respectively. The kind collaboration of ReSHEALience partner Penetron Italia (MArch. EnricoMaria Gastaldo Brac) in supplying the crystalline self-healing promoter is also acknowledged. The authors also thank Mr. Marco Francini (BuzziUnicem) for supplying of cement CEM I and dr Fulvio Canonico (BuzziUnicem Dyckerhoff) for supplying of cement CEM III, Mr. Michele Gadioli and Roberto Rosignoli (Azichem ltd) for supplying of steel fibres, dr Florian Bernard (Saint-Gobain Seva) for supplying of amorphous fibres and Mr. Sandro Moro (BASF Italia) for supplying the superplasticizer employed for casting the investigated mixes.

Funding Open access funding provided by Politecnico di Milano within the CRUI-CARE Agreement.

Data availability Some or all data, models, or code that support the findings of this study are available from the corresponding author upon reasonable request.

References

1. Bribián IZ, Capilla AV, Usón AA (2011) Life cycle assessment of building materials: Comparative analysis of energy and environmental impacts and evaluation of the eco-efficiency improvement potential. Build Environ 46(5):1133–1140
2. Banthia N (2008) Fiber reinforced concrete for sustainable and intelligent infrastructure. In: proceedings of the of first international conference on micro-structure related durability of cementitious composites. Rilem, Nanjing
3. Mackechnie JR, Alexander MG (2009) Using durability to enhance concrete sustainability. J Green Build 4(3):52–60. https://doi.org/10.3992/jgb.4.3.52
4. Al-Obaidi S, Bamonte P, Luchini M, Mazzantini I, Ferrara L (2020) Durability-based design of structures made with UHP/UHDC in extremely aggressive scenarios: application to a geothermal water basin case study. MDPI Infrastruct 5(11):1–44
5. Hafez H, Malchiodi B, Tošić N, Drewniok M, Purnell P, de la Fuente A (2024) Decarbonization potential of steel fibre-reinforced limestone calcined clay cement concrete one-way slabs. Constr Build Mater 435:136847. https://doi.org/10.1016/j.conbuildmat.2024.136847
6. Wille K, Parra-Montesinos GJ (2012) Effect of beam size, casting method, and support conditions on flexural behavior of ultra-high-performance fiber-reinforced concrete. ACI Mater J 109(3):379–388
7. Wille K, Kim DJ, Naaman AE (2011) Strain-hardening UHP-FRC with low fiber contents. Mater Struct/Mater Constr 44(3):583–598. https://doi.org/10.1617/s11527-010-9650-4
8. Wille K, Naaman AE, El-Tawil S, Parra-Montesinos GJ (2012) Ultra-high performance concrete and fiber reinforced concrete: achieving strength and ductility without heat curing. Mater Struct/Mater Constr 45(3):309–324. https://doi.org/10.1617/s11527-011-9767-0
9. Colombo M, Conforti A, di Prisco M, Leporace-Guimil B, Plizzari G, Zani G (2023) The basis for ductility evaluation in SFRC structures in MC2020: an investigation on slabs and shallow beams. Struct Concr 24(4):4406–4423. https://doi.org/10.1002/suco.202300114
10. de Andrade GG, de Figueiredo AD, Galobardes I, da Silva MAAP, de la Fuente A, Bitencourt LAG Jr. (2024) Experimental and numerical investigation of flexural behavior of precast tunnel segments with hybrid reinforcement. Tunnell Undergr Space Technol 154:106094. https://doi.org/10.1016/j.tust.2024.106094
11. Patel D, Pleesudjai C, Bui V, Pridemore P, Schaef S, Mobasher B (2023) Mechanical response of precast tunnel segments with steel and synthetic macro-fibers. Cem Concr Compos 144:105303. https://doi.org/10.1016/j.cemconcomp.2023.105303
12. Patel D, Pleesudjai C, Bakhshi M, Nasri V, Mobasher B (2025) Back-calculation of mechanical properties of fiber-reinforced concrete in tunnel lining segments. Struct Concr. https://doi.org/10.1002/suco.70052
13. Monteiro VMDA, Cardoso DCT, Silva FDA, Mobasher B (2024) The influence of steel fibers on the bond slip behavior between rebars and concrete: Experimental and analytical investigation. Constr Build Mater 411:134357. https://doi.org/10.1016/j.conbuildmat.2023.134357
14. Leporace-Guimil B, Conforti A, Plizzari GA (2025) Evaluation of orientation factors influencing the shear and flexural behavior of elements in steel fiber reinforced concrete. Constr Build Mater 474:141054. https://doi.org/10.1016/j.conbuildmat.2025.141054
15. Conforti A, Cuenca E, Zerbino R, Plizzari GA (2022) Influence of fiber orientation on the behavior of fiber reinforced concrete slabs. Struct Concr 22(3):1831–1844
16. Hernández Fraile D, Faccin E, Minelli F, Plizzari G, Muttoni A (2024) Fibre orientation in SFRC slabs and consequences for punching shear and flexural resistance. Eng Struct 302:117364. https://doi.org/10.1016/j.engstruct.2023.117364
17. Sadrolodabaee P, Claramunt J, Ardanuy M, de la Fuente A (2021) Mechanical and durability characterization of a new textile waste micro-fiber reinforced cement composite for building applications. Case Stud Constr Mater 14:e00492. https://doi.org/10.1016/j.cscm.2021.e00492
18. Van Der Putten J, Lesage K, De Schutter G (2016) Influence of the particle shape on the packing density and pumpability of UHPC. In: International symposium on ultra high performance concrete, March 2016
19. Khayat KH, Meng W, Vallurupalli K, Teng Le (2019) Rheological properties of ultra-high-performance concrete — an overview. Cem Concr Res 124:105828

20. Martinie L, Rossi P, Roussel N (2013) Rheology of fiber-reinforced cementitious materials: basic concepts and application to UHPFRC, Designing and Building with UHPFRC, pp 575–578
21. Li VC, Stang H, Krenchel H (1993) Micromechanics of crack bridging in fibre-reinforced concrete. Mats Structs 26(8):486–494
22. Li VC (2003) On engineered cementitious composites. A review of the material and its applications. J Adv Concr Tech 1(3):215–230
23. Cuenca E, Mezzena A, Ferrara L (2021) Synergy between crystalline admixtures and nano-constituents in enhancing autogenous healing capacity of cementitious composites under cracking and healing cycles in aggressive waters. Constr Build Mater 266(Part B):121447
24. Cuenca E, D'Ambrosio L, Lizunov D, Tretjakov A, Volobujeva O, Ferrara L (2021) Mechanical properties and self-healing capacity of Ultra High Performance Fibre Reinforced Concrete with alumina nanofibers: tailoring Ultra High Durability Concrete for aggressive exposure scenarios. Cem Concr Compos, 103956
25. Cuenca E, Criado M, Gimenez M, Alonso MC, Ferrara L (2022) Effects of alumina nanofibers and cellulose nanocrystals on durability and self-healing capacity of ultrahigh-performance fiber-reinforced concretes. ASCE J Mater Civ Eng 34(8):04022154
26. Plagué T, Desmettre C, Charron J-P (2017) Influence of fiber type and fiber orientation on cracking and permeability of reinforced concrete under tensile loading. Cem Concr Res 94:59–70
27. Zhang Z, Qian S, Ma S (2014) Investigating mechanical properties and self-healing behavior of micro-cracked ECC with different volume of fly ash. Constr Build Mater 52:17–23
28. Marangon E, Mobasher B, Fernandes WD, Silva FDA, Rambo DAS, Battista RC, Fairbairn EMR, Toledo Filho RD (2025) Experimental investigation of tension stiffening in hybrid reinforced concrete ties. Constr Build Mater 458:139505. https://doi.org/10.1016/j.conbuildmat.2024.139505
29. Martinello Carlesso D, Cavalaro SHP, Bairán JM, de la Fuente A (2025) Flexural fatigue performance of pre-cracked steel fibre reinforced concrete: Experimental program and design-oriented approach. Constr Build Mater 467:140308. https://doi.org/10.1016/j.conbuildmat.2025.140308
30. Snoeck D, De Belie N (2016) Repeated autogenous healing in strain-hardening cementitious composites by using superabsorbent polymers. J Mater Civ Eng 28(1):1–11
31. Baby F, Graybeal B, Marchand P, Toutlemonde F (2013) UHPFRC tensile behavior characterization: inverse analysis of four-point bending test results. Mater Struct 46:1337–1354
32. Qian S, Li VC (2007) Simplified inverse method for determining the tensile strain capacity of strain hardening cementitious composites. J Adv Concr Technol 5:235–246
33. Soranakom C, Mobasher B (2007) Closed-form moment-curvature expressions for homogenized fiber-reinforced concrete. ACI Mater J 104:351–359
34. López JÁ, Serna P, Navarro-Gregori J, Camacho E (2015) An inverse analysis method based on deflection to curvature transformation to determine the tensile properties of UHPFRC. Mater Struct 48:3703–3718
35. Mezquida-Alcaraz EJ, Navarro-Gregori J, Serna-Ros P (2021) Direct procedure to characterize the tensile constitutive behavior of strain-softening and strain-hardening UHPFRC. Cem Concr Compos 115:103854
36. López JÁ, Serna P, Navarro-Gregori J, Coll H (2016) A simplified five-point inverse analysis method to determine the tensile properties of UHPFRC from un-notched four-point bending tests. Compos B 91:189–204
37. Mezquida-Alcaraz EJ, Navarro-Gregori J, Angel Lopez J, Serna-Ros P (2019) Validation of a non-linear hinge model for tensile behavior of UHPFRC using a finite element model. Comput Concr 23:11–23
38. MC (2010) fib Model Code for Concrete Structures 2010, Comité Euro-International du Béton, Lausanne (Switzerland), 2012
39. Di Prisco M, Ferrara L, Lamperti MGL (2013) Double edge wedge splitting (DEWS): an indirect tension test to identify post-cracking behaviour of fibre reinforced cementitious composites. Mater Struct 46(11):1893–1918
40. Tahwia AM, Elgendy GM, Amin M (2022) Mechanical properties of affordable and sustainable ultra-high-performance concrete. Case Stud Constr Mater 16:e01069
41. Tahwia AM, Elgendy GM, Amin M (2022) Effect of environmentally friendly materials on steel corrosion resistance of sustainable UHPC in marine environment. Struct Eng Mech 82(2):133–149
42. Kurpińska M, Wcisło A (2022) Assessment of the application of CEM III with exposed aggregate as an alternative to CEM I for road pavements. Arch Civil Eng 68(2):461–481
43. Collepardi M, Collepardi S, Troli R (2022) Mix-Design of a Long-Term Durable Concrete for the Reinforced Foundations in the Bridge on the Straits of Messina, Italy. American Concrete Institute, ACI Special Publication, SP-355, pp 413–422
44. Almasailam F, Purnell P, Black L (2025) Factors affecting the carbon footprint of reinforced concrete structures. Mater Struct/Mater Constr 58(4):116
45. Tahwia AM, Elgendy GM, Amin M (2021) Durability and microstructure of eco-efficient ultra-high-performance concrete. Constr Build Mater 303:124491
46. Jiang C, Wang Y, Guo W, Jin C, Wei M (2018) Experimental study on the mechanical properties of amorphous alloy fiber-reinforced concrete. Adv Mater Sci Eng 2018:2395083. https://doi.org/10.1155/2018/2395083
47. Wang D, Liu R, Wang S, Ma X (2024) Mechanical properties of ultra-high-performance concrete with amorphous alloy fiber: surface modification by silane coupling agent KH-550. Materials 17(16):4037. https://doi.org/10.3390/ma17164037
48. Li Y, Deng YG (2021) "Mechanical properties and corrosion resistance of high performance fiber-reinforced concrete with steel or amorphous alloy fibers." Mater Res Express 8(9):095201. https://doi.org/10.1088/2053-1591/ac2698
49. Yoo DY, Banthia N, Yang JM, Yoon YS (2016) Size effect in normal- and high-strength amorphous metallic and

steel fiber reinforced concrete beams. Constr Build Mater 121:676–685
50. Yoo DY, Banthia N (2016) Experimental and numerical analysis of the flexural response of amorphous metallic fiber reinforced concrete. Mater Struct 64(50):64
51. Yang JM, Kim JK, Yoo DY (2017) Performance of shotcrete containing amorphous fibers for tunnel applications. Tunnelling Undergr Space Technol 64:85–94
52. Kim JH, Bae SH, Choi SJ (2021) Effect of amorphous metallic fibers on strength and drying shrinkage of mortars with steel slag aggregate. Materials 14(18):5403
53. Javed A, Gillani SAA, Abbass W, Riaz MR, Hameed R, Abbas S, Salmi A, Deifalla AF (2022) Mechanical performance of amorphous metallic fiber-reinforced and rubberized thin bonded cement-based overlays. Sustainability 14(13):8226
54. Yang JM, Yoon SH, Choi SJ, Kim GD (2013) Development and application of pig iron based amorphous fiber for concrete reinforcement. Magn Korea Concr Inst 25(4):38–41
55. Wu Z, Jia Y, Jin Z, Ren H, Ni X (2020) The corrosion behaviour of amorphous metal fiber compared with that of stainless steel fiber. In: Journal of physics: conference series, Volume 1637, 8th annual international conference on material science and engineering (ICMSE2020) August 14–15, Guiyang, Guizhou, China
56. Xiao S, Guo S (2021) Research progress on extreme wettability of amorphous alloy surface. Surf Tech 50:101–111
57. Wang D, Liu R, Wang S, Ma X (2024) Mechanical properties of ultra-high-performance concrete with amorphous alloy fiber: surface modification by silane coupling agent KH-550. Materials 17:4037
58. Shaikh FUA, Kahlon NS, Dogar AUR (2023) Temperature on the behavior of amorphous metallic fibre-reinforced cement and geopolymer composites. Fibers 11:31
59. Lo Monte F, Ferrara L (2021) Self-healing characterization of UHPFRCC with crystalline admixture: Experimental assessment via multi-test/multi-parameter approach. Constr Build Mater 283:122579
60. Cuenca E, Lo Monte F, Moro M, Schiona A, Ferrara L (2021) Effects of autogenous and stimulated self-healing on durability and mechanical performance of UHPFRC: Validation of tailored test method through multi-performance healing-induced recovery indices. Sustainability 13(20):11386
61. Lo Monte F, Ferrara L (2020) Tensile behaviour identification in ultra-high performance fibre reinforced cementitious composites: indirect tension tests and back analysis of flexural test results. Mater Struct. https://doi.org/10.1617/s11527-020-01576-8
62. Al Obaidi S, Bamonte P, Animato F, Lo Monte F, Mazzantini I, Luchini M, Scalari S, Ferrara L (2021) Innovative design concept of cooling water tanks/basins in geothermal power plants using ultra high performance fiber reinforced concrete with enhanced durability. MDPI Sustain 13(17):1–26
63. Al-Obaidi S, Davolio M, Lo Monte F, Costanzi F, Luchini M, Bamonte P, Ferrara L (2022) Structural validation of geothermal water basins constructed with durability enhanced ultra high performance fiber reinforced concrete (Ultra High Durability Concrete). Case Stud Constr Mater 17:e01202
64. Lopez JA, Serna P, Camacho E, Coll H, Navarro-Gregori J (2014) First ultra-high-performance fibre-reinforced concrete footbridge in Spain: design and construction. Struct Eng Int 24(1):101–104
65. Dadvar SA, Mostofinejad D, Bahmani H (2020) Strengthening of RC columns by ultra-high performance fiber reinforced concrete (UHPFRC) jacketing. Constr Build Mater 235:117485
66. Meda A, Mostosi S, Riva P (2014) “Shear strengthening of reinforced concrete beam with high-performance fiber-reinforced cementitious composite jacketing.” ACI Struct J 111(5):1059–1067. https://doi.org/10.14359/51686807
67. DIANA (Software) . (2017) User’s Manual - Release 10.2, TNO DIANA, Netherlands https://dianafea.com/manuals/d102/Diana.html
68. Li Y, Deng YG (2021) Mechanical properties and corrosion resistance of high performance fiber-reinforced concrete with steel or amorphous alloy fibers. Mater Res Express 8(9):095201
69. Accornero F, Rubino A, Carpinteri A (2020) Ductile-to-brittle transition in fiber-reinforced concrete beams: Scale and fiber volume fraction effects. Mater Des Process Commun. https://doi.org/10.1002/mdp2.127
70. Davolio M, Al-Obaidi S, Altomare MY, Lo Monte F, Ferrara L (2023) A methodology to assess the evolution of mechanical performance of UHPC as affected by autogenous healing under sustained loadings and aggressive exposure conditions. Cem Concr Compos 139:105058
71. Al-Obaidi S, Davolio M, Recchia G, Lo Monte F, Ferrara L (2023) How does self-healing under sustained loadings in aggressive water affect the constitutive response of a UHPFRC?. Special Collection of SHCC5, RILEM Bookseries (39) Strain Hardening Cementitious Composites
72. Al-Obaidi S, He S, Schlangen E, Ferrara L (2023) Effect of matrix self-healing on the bond-slip behavior of micro steel fibers in ultra high-performance concrete. Mater Struct 56:161
73. Lo Monte F, Repesa L, Snoeck D, Doostkami H, Roig-Flores M, Jackson SJP, Alvarez AB, Nasner M, Borg RP, Schröfl C, Giménez M, Alonso MC, Serna P, De Belie N, Ferrara L (2024) Multi-performance experimental assessment of autogenous and crystalline admixture-stimulated self-healing in UHPFRCCs: Validation and reliability analysis through an inter-laboratory study. Cem Concr Compos 145:105315